Breaking Rotational Symmetry in Supertwisted WS$_2$ Spirals via Moiré Magnification of Intrinsic Heterostrain

Penghong Ci,[#] Yuzhou Zhao,[#] Muhua Sun,[#] Yoonsoo Rho, Yabin Chen, Costas P. Grigoropoulos, Song Jin, Xiaoguang Li,* and Junqiao Wu*

Read Online

ACCESS | Metrics & More | Article Recommendations | Supporting Information

ABSTRACT: Twisted stacking of van der Waals materials with moiré superlattices offers a new way to tailor their physical properties via engineering of the crystal symmetry. Unlike well-studied twisted bilayers, little is known about the overall symmetry and symmetry-driven physical properties of continuously supertwisted multilayer structures. Here, using polarization-resolved second harmonic generation (SHG) microscopy, we report threefold (C_3) rotational symmetry breaking in supertwisted WS$_2$ spirals grown on non-Euclidean surfaces, contrasting the intact symmetry of individual monolayers. This symmetry breaking is attributed to a geometrical magnifying effect in which small relative strain between adjacent twisted layers (heterostrain), verified by Raman spectroscopy and multiphysics simulations, generates significant distortion in the moiré pattern. Density-functional theory calculations can explain the C_3 symmetry breaking and unusual SHG response by the interlayer wave function coupling. These findings thus pave the way for further developments in the so-called "3D twistronics".

KEYWORDS: *twistronics, second harmonic generation, supertwisted spiral, symmetry breaking, moiré superlattice*
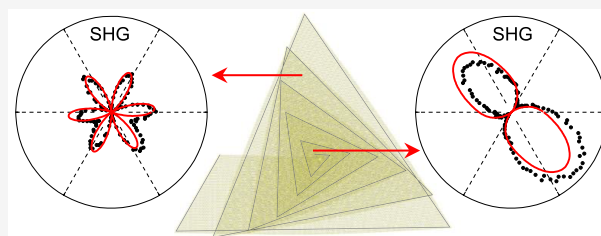
Overlaying atomic layers of two-dimensional (2D) van der Waals (vdW) materials creates moiré superlattices, which have a microstructure controlled by the interlayer twist angle between adjacent layers. This strategy provides a fundamentally new paradigm for breaking and engineering crystal symmetries, thereby manipulating the internal quantum degrees of freedom and leading to numerous extraordinary physical phenomena.[1,2] By controlling the spontaneous symmetry breaking in magic-angle moiré patterns, semimetallic bilayer graphene can be transformed into a succession of unconventional electronic phases, such as superconductors,[3] quantum anomalous Hall Insulators,[4] and Mott-like correlated insulators.[5] In transition metal dichalcogenides (TMD) heterostructure superlattices, moiré excitons,[6–8] Mott insulator states,[9] and Wigner crystallization have been observed experimentally,[9] along with modulation of the local atomic configuration with threefold (C_3) rotational symmetry and energy extrema within the moiré supercell.[7]

Beyond well-studied twisted bilayers, interest in twisted multilayer systems has been growing, because the additional twist angles between each pair of neighboring layers offer a new degree of freedom to allow further manipulation of symmetry breaking and electron correlations.[10–12] As a result of the interference between two bilayer moiré cells in the twisted multilayer systems, the formation of higher-order "moiré of moiré" leads to longer period superstructure which reveals more fascinating and robust physical properties.[13,14] For example, recently, twisted trilayer and multilayer graphene

have been reported to exhibit a broader range of magic angles and higher transition temperatures of superconductivity than twisted bilayer graphene.[15,16] In TMD systems, compared to WS$_2$/WSe$_2$ heterostructure, graphene/WS$_2$/WSe$_2$ superlattices reportedly show deeper moiré potential and stronger interlayer coupling.[17] Theoretical studies have revealed fascinating physical properties in continuously twisted multilayer systems, forming the basis for "3D twistronics";[18,19] for example, quantum geometry has been predicted to govern super-conductivity and superfluidity in platforms including, but not limited to, twisted multilayer graphene.[10] However, the "tear-and-stack" technique, the most prevalent way to fabricate twisted 2D structures, has limited capability and throughput for creating 3D twistronics.[20,21] In light of this limitation, direct synthesis of continuously twisted TMD structures, termed "supertwisted spirals", has been achieved via screw dislocation driven growth on non-Euclidean surfaces.[11]
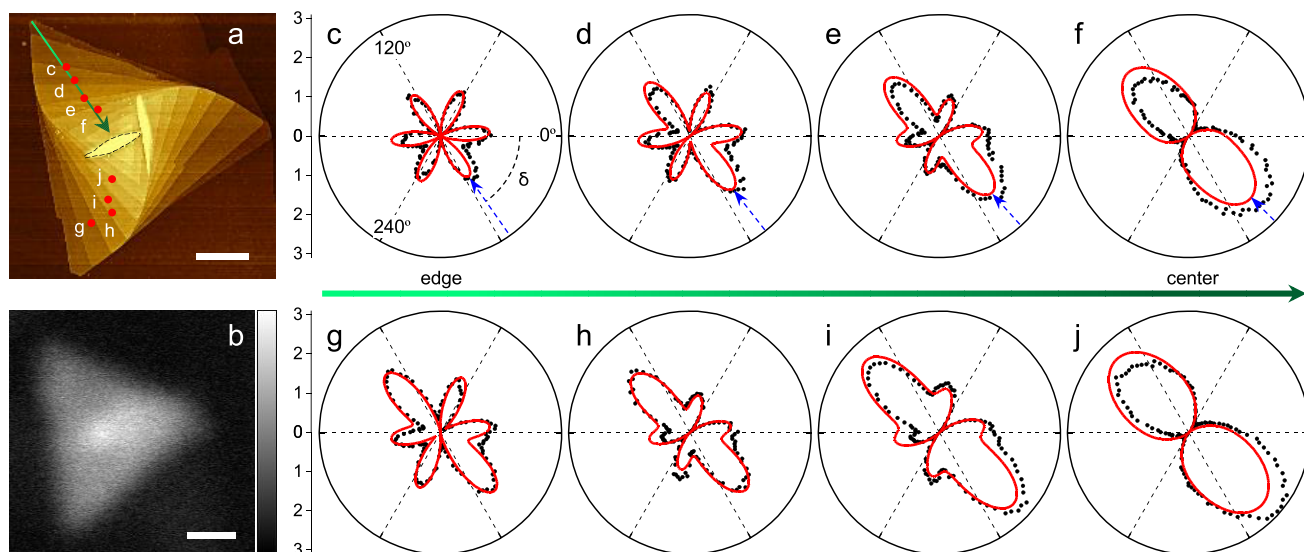
The presence of screw dislocations and curved substrates disrupts the perfect crystalline periodicity, thereby inducing a native strain field in supertwisted spirals.[11,22] A relative strain between adjacent twisted layers (heterostrain) can anisotropi-
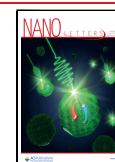
**Figure 1.** C_3 rotational symmetry breaking near the center of a representative supertwisted WS$_2$ spiral. (a) and (b) AFM and nonpolarized SHG intensity mapping images of a supertwisted WS$_2$ spiral grown around a WO$_x$ particle (marked by the black dashed line in panel (a) on SiO$_2$/Si substrate (scale bar: 1 μm). (c)−(j) Polarization-resolved SHG intensity patterns at various positions labeled in panel (a), which gradually evolve from the six-petal into two-lobe symmetry along the green arrow. The incident laser and the SH electric field were linearly copolarized while rotating together relative to the sample plane. The azimuthal angle of 0° refers to incident laser polarization parallel to the horizontal direction in panel (a). Black symbols are experimental data; red curves are fitted via a modified bond additive model (Figure 5); blue arrows indicate the average "armchair" orientations at each measurement position.
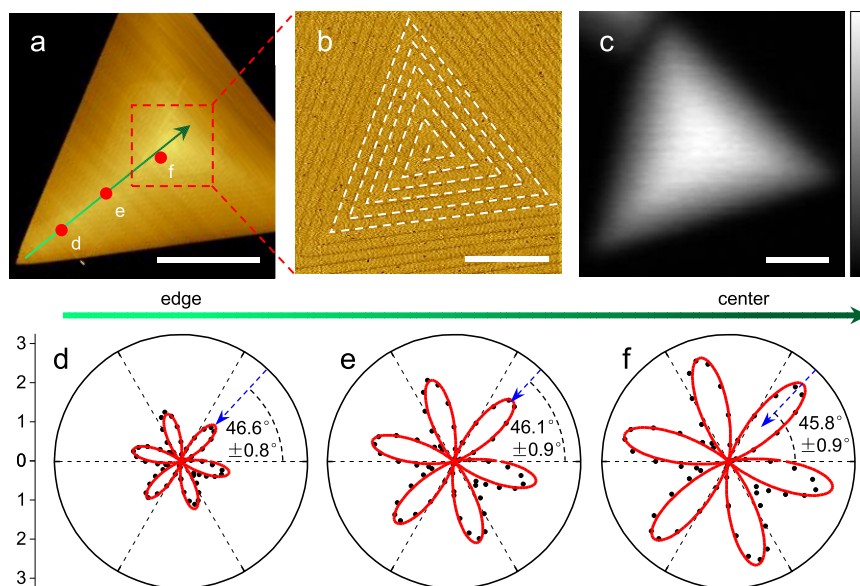
Figure 2. The persistence of C_3 rotational symmetry in a representative aligned WS$_2$ spiral. (a)−(c) AFM and nonpolarized SHG mapping images of an aligned WS$_2$ spiral grown on a flat substrate. The zoomed-in AFM image in panel (b) shows the trace out of the dislocation spiral in the white dashed line. Scale bars: 2 μm, 0.5 μm, and 1.5 μm, respectively. (d)−(f) Polarization-resolved SHG intensity patterns at various positions labeled in panel (a), exhibiting a characteristic sixfold symmetry and thus confirming the C_3 rotational symmetry in the entire sample. Black symbols are experimental data; red curves are fitted via SH field superposition theory; blue arrows indicate the armchair direction of the sample.

cally affect superlattice wavelengths, known as the moiré magnification effect.[23−25] This effect manifests as a dramatic distortion of the moiré pattern deviating from the hexagonal shape and hence leads to modifications of symmetry-related properties.[23,24,26,27] Yet, the symmetry evolution in super-twisted spirals modulated by the combination of moiré superlattice and native strain remains unclear, impeding further understanding of their physical properties. Second harmonic generation (SHG) sensitive to electric dipoles in non-

centrosymmetric systems is a powerful tool to probe symmetry-related physical properties that are otherwise challenging to study.[28,29] Therefore, it is intriguing and essential to investigate whether supertwisted structures with intrinsic heterostrain possess abnormal symmetry breaking that can be probed by azimuthal polarization of SHG intensity. The answer is not straightforward, as tiny lattice deformation would not significantly change the symmetry of the system. For this reason, the traditional superposition theory of the second
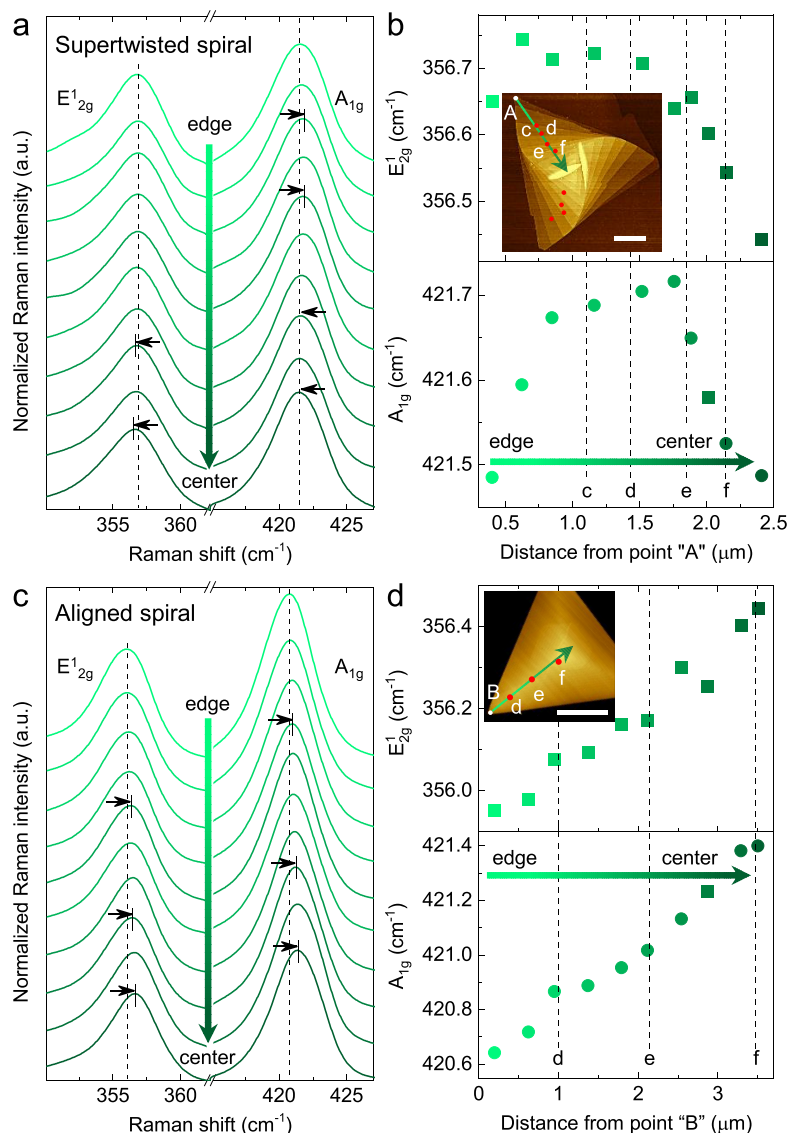
Figure 3. Probing strain magnitude in supertwisted WS$_2$ spiral. (a) and (c) Raman spectra of a supertwisted and an aligned WS$_2$ spiral along the green arrows in their respective AFM images (the insets in panels (b) and (d)). The dashed lines represent the peaks of the two phonon modes of the sample in the edge region. The black arrows show the redshift or blueshift of Raman peaks. (b) and (d) Individual E$^1_{2g}$ and A$_{1g}$ mode frequencies of supertwisted and aligned WS$_2$ spiral as a function of the distance from point "A" or "B" labeled in their respective AFM images (insets). The dashed lines indicate the positions where the SHG patterns were recorded in Figures 1 and 2. Scale bars for (b) and (d) are 1 and 2 μm, respectively. When approaching the center of the spiral, frequencies of both E$^1_{2g}$ and A$_{1g}$ modes monotonically increase in the aligned spiral due to the increase in the number of WS$_2$ layers. However, the frequencies drop near the center of the supertwisted spiral, indicating intrinsic and nonuniform strain in the supertwisted spiral.

harmonic (SH) field would expect the SHG patterns of TMDs to be symmetric six petals with slight distortion when twist and strain are simultaneously tuned.[30−34]

Here, we report a C_3 rotational symmetry breaking in supertwisted WS$_2$ spirals revealed by polarization-resolved SHG, in contrast to the intrinsic C_3 rotational symmetry of aligned WS$_2$ layers. The relative strain between neighboring layers, demonstrated by the redshift of Raman peaks and multiphysics simulations, is magnified by the moiré superlattice and thus breaks the overall C_3 rotational symmetry. Fundamentally, the overall symmetry breaking of electronic structure is caused by the strongly asymmetric charge density differences in the moiré supercell arising from a nontrivial interlayer coupling. We also developed a modified bond additivity model to simulate the effect of heterostrain and

distorted moiré superlattice on the SHG patterns, which shows good agreement with the experimental SHG results for supertwisted spirals.

The synthesis and detailed structural characterization of the twisted WS$_2$ spirals studied herein were described previously.[11] Figure 1a presents an atomic force microscopy (AFM) image of a "fastened" WS$_2$ spiral with a right-handed twisted superstructure. This fastened spiral was grown on a protruded substrate, where the center of the screw dislocation sits above a protrusion denoted by the dashed line near the center of Figure 1a. Based on the non-Euclidean twist mechanism we previously reported,[11] the crystal lattice twist is consistent with the geometric twist of the layers. Consequently, the shape of the spiral is bent following the protrusion's curvature, which inevitably introduces nonuniform strain into the system. To
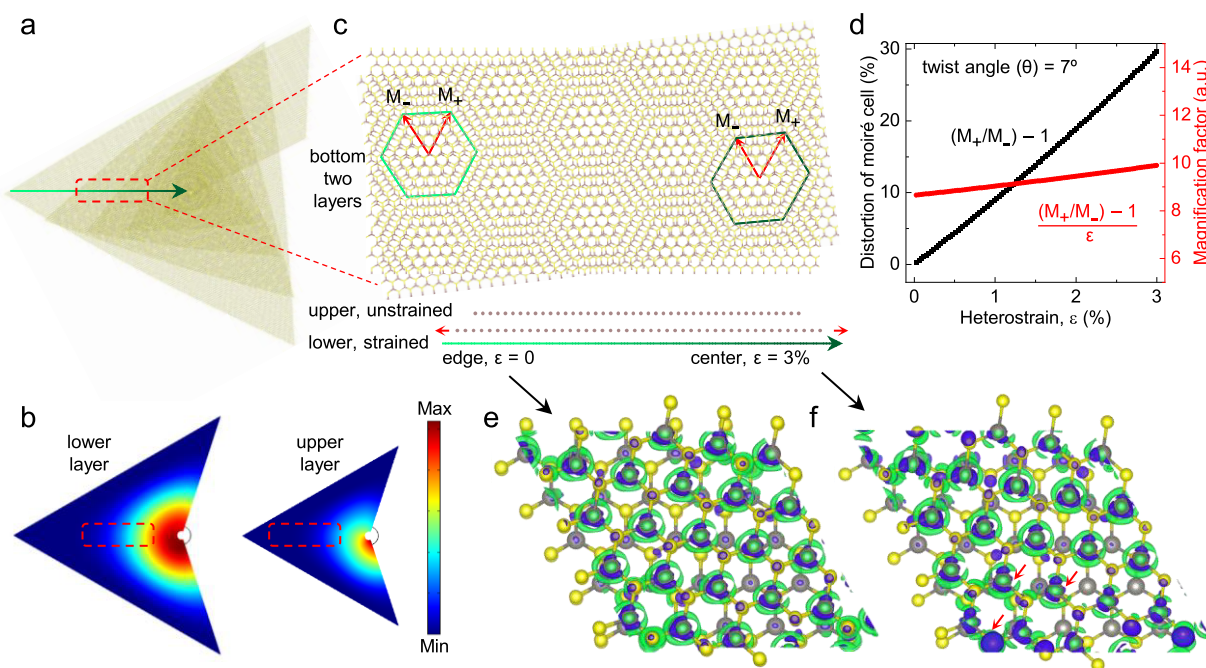
Figure 4. Symmetry transition induced by moiré magnification of intrinsic heterostrain in the supertwisted TMD spiral. (a) Schematic of a non-Euclidean supertwisted TMD spiral following the structure of the AFM image in Figure 1a. (b) Deformation of the bottom two layers qualitatively simulated by COMSOL (see details in Figure S4) increases from the edge of the spiral to its center. Compared to the lower layer, the tensile strain magnitude of the upper layer is so small that it is disregarded inside the red dashed rectangle, while the symmetry transition of the moiré pattern is investigated in (c). The upper layer is unstrained, but the lower layer undergoes enhanced strain (along the zigzag direction) from the edge to the center, leading to the broken C_3 rotational symmetry of the moiré pattern (the dark green elongated hexagon), which is consistent with the two-lobe SHG patterns in Figure 1f,j. (d) Calculated length distortion ($M_+/M_- - 1$) between two vectors of the moiré supercell and the magnification factor (($M_+/M_- - 1$)/ε) as a function of relative tensile strain (ε) between neighboring twisted layers. (e) and (f) DFT calculated charge density differences in the moiré supercell (twist angle of ~7°) without strain and with tensile heterostrain of ~3% (along zigzag direction), corresponding to the edge and the center of the spiral, respectively. Brown and yellow spheres represent W and S atoms, respectively. The blue and green areas represent electron accumulation and depletion due to the interlayer charge transfer. The red arrows show some localized regions with nonuniform distribution of charge density. The magnifying effect of the moiré pattern on heterostrain, combined with interlayer hybridization, strongly distorts the symmetry of charge density.

explore the resultant potential symmetry modification of this spiral, we performed nonlinear SHG (2ω) characterization using a pulsed femtosecond laser with a fundamental wavelength (ω) of 800 nm (see details in Methods and Figure S1). Figure 1b shows the SHG microscopy image of the same area in Figure 1a by raster scanning the sample, indicating the breaking of inversion symmetry over the entire sample.

After eliminating the impact of oblique incidence on SHG response (see Note 1 in SI), we further measured the azimuthal polarization-resolved SHG intensity patterns of this supertwisted WS$_2$ spiral at different points of the supertwisted spiral (Figure 1c-j). Surprisingly, when approaching the spiral core, the SHG patterns transform from the normal six symmetric petals to an abnormal dumbbell shape. In stark contrast, aligned WS$_2$ spirals grown on flat surfaces possess a 3R-like stacking geometry with an 0° interlayer twist, illustrated by the AFM image (Figure 2a,b) and previous studies,[35−37] and exhibit undistorted six-petal polarization-resolved SHG intensity patterns everywhere (Figure 2d-f), independent of the measurement positions. This suggests that, unlike the aligned spiral, unexpected symmetry breaking occurs in the supertwisted spiral.

We start with analyzing the azimuthal polarization-resolved SHG intensity patterns by the superposition theory of the SH field,[33,38,39] the most widely used model to fit the SHG response in twisted TMDs. Monolayer TMDs, belonging to

the noncentrosymmetric D_{3h} point group, have a threefold rotation axis perpendicular to the surface.[30] Thus, upon normal incidence, when the excitation polarizer is parallel to the SHG signal analyzer, the SHG intensity (I) pattern is known to exhibit sixfold rotational symmetry (Figure S1). This process is expressed as $I \propto |\vec{E}_{2\omega}|^2 \propto |\cos 3\phi|^2$, in which $\vec{E}_{2\omega}$ and ϕ are the SH electric field and the polarization angle of the laser, respectively.[30,40] For stacked bilayers with a twist angle θ, the total SH field ($\vec{E}_{2\omega}^T$) is the vector addition of dipole moments ($\vec{E}_{2\omega}^1$ and $\vec{E}_{2\omega}^2$) from two electrically decoupled layers: $\vec{E}_{2\omega}^T = \vec{E}_{2\omega}^1 + \vec{E}_{2\omega}^2 \propto \cos 3\phi + \cos 3(\phi + \theta)$.[33,41] The total SHG intensity of the twisted bilayers depends on the twist angle, but the SHG patterns preserve sixfold symmetry as reported in the literature.[33] When expanding this theory to the twisted multilayers, the material absorption for the first to the N-th layer is taken into account to obtain the SH field from the N-th layer,[42] and we found that the six-petal SHG pattern remains, as illustrated in simulations (Figure S2). Therefore, if only considering the degree of freedom of twist, the conventional SH field superposition theory cannot explain the two-lobe SHG patterns observed near the center of the supertwisted spirals. We need to note that, unlike the twisted structures fabricated by the "tear-and-stack" technique, the supertwisted spiral is natively deformed by the underlying protrusion during the growing process, thus introducing an additional degree of strain to contribute to symmetry-related physical properties.

To probe and estimate the strain magnitude, we measured the Raman spectra of supertwisted (Figure 3a,b) and aligned WS$_2$ spirals (Figure 3c,d) at various points using a 488 nm laser excitation (see details in Methods). In the aligned spiral, both in-plane (E^1_{2g}) and out-of-plane (A_{1g}) Raman vibrational modes monotonically rise from the edge to the center because of the increase in the thickness.[43] In contrast, the supertwisted spiral exhibits a redshift of the E^1_{2g} and A_{1g} peaks at positions near the center (Figure 3a,b), indicating the existence of nonuniform strain magnitude that compensates for the stiffened vibration caused by the increasing sample thickness.[44,45] In the next step, using the reported A_{1g} Raman shift rates ($\partial\omega(A_{1g})/\partial\varepsilon$) of 2H-stacked few-layer WS$_2$ as a function of strain ($\sim$0.74 cm^{-1}/% strain),[45] we estimate the tensile strain magnitude to be $\sim$0.4% around the position "f" in the supertwisted spiral. Note that in practice, the total strain must surpass 0.4% because the thickness-induced bond stiffening reduces strain-induced redshift of A_{1g} and the steric effect softens the atomic vibration for the randomly stacked TMDs, weakening the response of Raman mode to strain.[46]

We now turn to analyzing the role of strain in the SHG patterns of the supertwisted spiral. On the basis of the photoelastic effect, Mennel et al. demonstrated that the angular distribution of SHG intensity of monolayer TMDs under uniaxial strain is given by $I \propto \frac{1}{4}(A \cos 3\phi + B \cos(2\phi + \gamma))^2$, where A and B are related to the magnitude of strain and the photoelastic coefficients, respectively, and γ is the principal strain orientation.[31,47] Using a model based on a combination of Mennel's equation and the SH field superposition theory, even when the tensile strain magnitude reaches as high as $\sim$3%, the SHG patterns would only become distorted and still retain the six-petal shape, as calculated in Figure S3. This can be attributed to two primary reasons: (1) Raman spectroscopy has limited capability in detecting the independent strain of each layer, whereas the heterostrain plays a critical role in moiré strain engineering and symmetry-related properties;[24,48−52] (2) the theory of SH field superposition neglects the interlayer vdW interaction and models the SH response of individual layers as electrically decoupled layers, while interlayer hybridization of wave functions is known to modulate the overall symmetry and the resultant SHG patterns.[53,54]

The localized heterostrain in twisted TMD bilayers and their corresponding distorted moiré patterns have been observed using piezoresponse force microscopy.[49] For vdW materials with thickness greater than five layers, however, it is challenging to experimentally quantify the strain of each layer. Therefore, we use COMSOL multiphysics to simulate the influence of protrusion on the formation of the supertwisted spiral by applying a force beneath the spiral. Interestingly, the deformation increases from the top layer to the bottom layer (Figure 4a,b), suggesting the presence of heterostrain in the supertwisted spiral. This can be understood by the mechanism of the "non-Euclidean" twist,[11,12,55] in which the deformed upper layers tend to more easily relax via layer-to-layer sliding during the growing process of the supertwisted spirals because of the ultralow interfacial friction and weak interlayer forces in the vdW materials.[55,56]

For twisted 2D lattices under heterostrain, an angular distortion in the lattice vectors anisotropically modulates the moiré pattern in each direction.[23] As a result, the moiré pattern amplifies any small lattice deformation between neighboring

layers, known as the magnifying glass effect,[23,24,26,27] and the unit cells of the moiré superlattice can be distorted from hexagonal to oblique shape with a small heterostrain (Figures 4c and S5), modifying the lattice microstructure and consequently the electronic properties.[24] The extension of such a theory from twisted bilayers to supertwisted multilayers is challenging, due to the higher-order "moiré of moiré" superlattice formation and the much larger incommensurate system size.[13,14,57] Therefore, to simplify the treatment of a supertwisted structure, we investigate the moiré superlattice only in the bottom two layers of the supertwisted spiral, as illustrated by the dashed rectangle in Figure 4a,c. According to the numerically simulated deformation distribution, strain in the upper layer is negligibly small, but the lower layer experiences a higher, nonuniform strain, gradually increasing from the edge ($\varepsilon = 0$) to the center (assumed to be $\sim$3%) of the spiral. Owing to the low strain between the neighboring layers, the edge of the spiral retains C_3 rotational symmetry (the light green hexagon in Figure 4c), in good agreement with the observed sixfold SHG patterns in Figure 1c,g. On the other hand, for the center of the supertwisted spiral, the heterostrain (ε) is magnified in the moiré superlattice by a factor of $\sim(M_+/M_- - 1)/\varepsilon$. Here M_+ and M_- are the two vectors of the moiré supercell (Figures 4c and S5) and are defined by $M_{\pm} = \frac{a(1+\epsilon_{\pm})}{2\sqrt{(1+\epsilon_{\pm})\sin^2[(\theta + \varphi_{\pm})/2] + \epsilon_{\pm}^2/4}}$, where a is the in-plane lattice constant of the monolayer vdW material, $\epsilon_{\pm}$ are related to the strain matrix, and $\varphi_{\pm}$ are rotation angles of moiré vectors between twisted layers (see details in Figure S5).[23−25] For the moiré pattern with an interlayer twist angle of 7° (the case of the supertwisted spiral sample in Figure 1a), a nearly 1 order of magnitude magnification of small heterostrains imposed by the moiré pattern (Figure 4d) would completely break the C_3 rotational symmetry, as illustrated by the dark green distorted hexagon in Figure 4c (and Figure S5). This is in agreement with the observed two-lobe SHG patterns in Figure 1f,j.

We note that heterostrain-induced distortion of the moiré pattern in twisted systems is a necessary but not sufficient condition for obtaining a two-lobe SHG pattern.[53,54] It is also important to consider interlayer coupling which arises from the hybridization of wave functions (particularly the sulfur orbitals) from neighboring layers to form bonding and antibonding states.[58,59] Otherwise, the supertwisted spiral would inherit the band structure and SH fields from the individual layers, hence still generating a sixfold SHG pattern with some distortion, as predicted by the SH field superposition theory (Figure S3). To verify and explore the contribution of the interlayer coupling and charge transfer to electronic structure, we utilized density-functional theory (DFT) to calculate the charge density differences of an exemplary WS$_2$ bilayer superlattice with an interlayer twist of 7° (Figure 4e,f). The unstrained moiré pattern presents a uniform electron accumulation and depletion (Figure 4e), consistent with the sixfold SHG patterns in the edge of the supertwisted spiral (Figure 1c). In stark contrast, for the bilayer superlattice with a heterostrain of $\sim$3% (Figure 4f), the distortion of the moiré pattern generates an uneven charge density redistribution (denoted by red arrows as examples) due to the interfacial charge transfer, which breaks the overall C_3 rotational symmetry in the center of the supertwisted spiral and explains the observed two-lobe SHG patterns (Figure 1f,j). Indeed, following a similar reason, although SHG is forbidden for centrosymmetric monolayer graphene, exceptionally strong
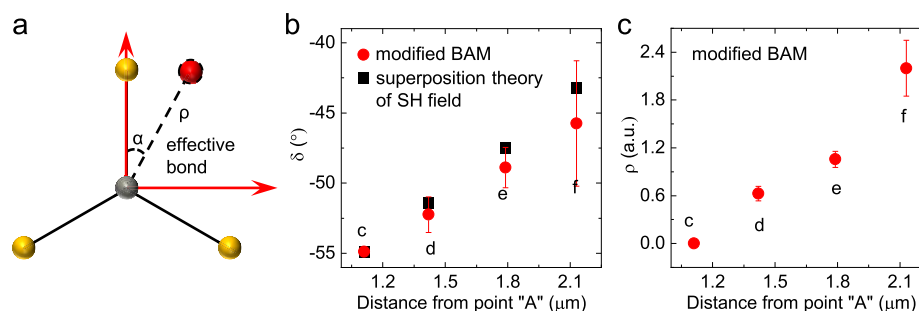
Figure 5. Modified bond additivity model (BAM) to fit SHG patterns of the supertwisted spiral. (a) Definition of coordinates for a triangular structural unit with an effective bond (red sphere) to derive the modified BAM (eq 1). Brown and yellow spheres represent W and S atoms, respectively. (b) and (c) Fitted parameters of δ (b) and ρ (c) as a function of distance for observed SHG patterns shown in Figure 1c-f.

SHG is allowed in ABA-stacked trilayer graphene, originating from the overall inversion symmetry breaking combined with a nontrivial interlayer wave function interaction.[28]

Finally, to fit the SHG patterns of the supertwisted spiral (Figure 1c-j), we employ the bond additivity model (BAM) that is typically used to model the SHG response in monolayer TMDs distorted with one tilted bond.[60,61] In the supertwisted spiral, the overall symmetry is modulated by the moiré magnification of heterostrain and results in a distorted moiré superlattice (Figure 4c,d), so a phenomenological approach can be employed by introducing an effective bond (Figure 5a) in the BAM to fit the C_3 rotational symmetry breaking. The SHG intensity pattern is given by the modified BAM (see Note 2 in SI):

$$I_{\text{SHG}} \propto \left| \frac{3}{4}\cos 3(\phi - \delta) + \rho e^{i\Theta}\cos^3(\phi - \delta - \alpha) \right|^2 \quad (1)$$

where α is the angle of the additional bond away from the vertical W−S bond, δ is the angle between average "armchair" orientations of the supertwisted spiral and the horizontal direction (blue arrows in Figure 1), and ρ and Θ are the change in the amplitude and phase of the dipole moment of the effective bond, respectively. Equation 1 fits well with the measured SHG patterns in Figure 1c-j. Figure 5b presents that the values of the fitted angle δ rise linearly from the edge of the spiral to its center, showing good consistency with the values extracted from the SH field superposition theory (Figure S2), indicating a continuously twisted structure. The enhancement of ρ toward the center of the spiral suggests a complete breaking of the C_3 symmetry for the SHG response.

In summary, we report a complete breaking of the original threefold rotational symmetry in supertwisted WS_2 spirals arising from a nearly 1 order of magnitude magnification of small heterostrains between neighboring twisted layers by the moiré pattern. Combined with an interlayer hybridization and charge transfer effect, such symmetry breaking leads to a complete change of the polarization-resolved SHG pattern. Our results open new ways to engineering moiré superlattices of vdW materials by generating continuously twisted multilayer systems (3D twistronics), suggesting new avenues for exploring flat bands, moiré excitons, and strongly correlated insulating states.[17] A wealth of intriguing symmetry-related physical effects are also potentially observed in the supertwisted spirals, such as enhanced intrinsic photovoltaic effect and in-plane anisotropy,[62,63] as the C_3 rotational symmetry breaking often results in anisotropic band structure and light−matter interactions.[1] From a broad perspective, the C_3 rotational symmetry breaking of the overall moiré pattern, together with the inversion symmetry breaking in individual TMD layers, may provide a general platform for studying various quantum geometrical phenomena, such as valley orbital magnetization,[64] valley magnetoelectricity,[65] and nonlinear Hall effects.[66,67]

■ ASSOCIATED CONTENT

ⓢ Supporting Information

The Supporting Information is available free of charge at https://pubs.acs.org/doi/10.1021/acs.nanolett.2c03347.

> More details for the sample synthesis and experimental setup; Figures S1−S5, Notes S1 and S2; SH field superposition theory; COMSOL multiphysics simulations; moiré magnification of heterostrain; modified bond additivity model (PDF)

■ AUTHOR INFORMATION

Corresponding Authors

Junqiao Wu − *Department of Materials Science and Engineering, University of California, Berkeley, California 94720, United States; Materials Sciences Division, Lawrence Berkeley National Laboratory, Berkeley, California 94720, United States;* ⓘ orcid.org/0000-0002-1498-0148; Email: wuj@berkeley.edu

Xiaoguang Li − *Institute for Advanced Study, Shenzhen University, Shenzhen 518060, China;* ⓘ orcid.org/0000-0001-9979-053X; Email: xgli@szu.edu.cn

Authors

Penghong Ci − *Department of Materials Science and Engineering, University of California, Berkeley, California 94720, United States; Materials Sciences Division, Lawrence Berkeley National Laboratory, Berkeley, California 94720, United States; Institute for Advanced Study, Shenzhen University, Shenzhen 518060, China*

Yuzhou Zhao − *Department of Chemistry, University of Wisconsin - Madison, Madison, Wisconsin 53706, United States*

Muhua Sun − *National Center for Electron Microscopy in Beijing, School of Materials Science and Engineering, Tsinghua University, Beijing 100084, China*

Yoonsoo Rho − *Department of Mechanical Engineering, University of California, Berkeley, California 94720, United States; Physical & Life Sciences and NIF & Photon Sciences, Lawrence Livermore National Laboratory, Livermore, California 94550, United States*

Yabin Chen − *School of Aerospace Engineering, Beijing Institute of Technology, Beijing 100081, China;* ⓘ orcid.org/0000-0002-5180-2009

Costas P. Grigoropoulos − *Department of Mechanical Engineering, University of California, Berkeley, California 94720, United States;* ⊙ orcid.org/0000-0002-8505-4037

Song Jin − *Department of Chemistry, University of Wisconsin - Madison, Madison, Wisconsin 53706, United States;* ⊙ orcid.org/0000-0001-8693-7010

Complete contact information is available at:
https://pubs.acs.org/10.1021/acs.nanolett.2c03347

Author Contributions

Notes

The authors declare no competing financial interest.

■ ABBREVIATIONS

SHG, second harmonic generation; C_3, threefold; SH, second harmonic; 2D, two-dimensional; vdW, van der Waals; TMD, transition metal dichalcogenides; AFM, atomic force microscopy; SH, second harmonic; DFT, density-functional theory; BAM, bond additivity model

■ REFERENCES

(1) Du, L.; Hasan, T.; Castellanos-Gomez, A.; Liu, G.-B.; Yao, Y.; Lau, C. N.; Sun, Z. Engineering symmetry breaking in 2D layered materials. *Nature Reviews Physics* **2021**, *3* (3), 193−206.

(2) Lau, C. N.; Bockrath, M. W.; Mak, K. F.; Zhang, F. Reproducibility in the fabrication and physics of moiré materials. *Nature* **2022**, *602* (7895), 41−50.

(3) Cao, Y.; Fatemi, V.; Fang, S.; Watanabe, K.; Taniguchi, T.; Kaxiras, E.; Jarillo-Herrero, P. Unconventional Superconductivity in Magic-Angle Graphene Superlattices. *Nature* **2018**, *556* (7699), 43−50.

(4) Serlin, M.; Tschirhart, C.; Polshyn, H.; Zhang, Y.; Zhu, J.; Watanabe, K.; Taniguchi, T.; Balents, L.; Young, A. Intrinsic quantized anomalous Hall effect in a moiré heterostructure. *Science* **2020**, *367* (6480), 900−903.

(5) Cao, Y.; Fatemi, V.; Demir, A.; Fang, S.; Tomarken, S. L.; Luo, J. Y.; Sanchez-Yamagishi, J. D.; Watanabe, K.; Taniguchi, T.; Kaxiras, E. Correlated insulator behaviour at half-filling in magic-angle graphene superlattices. *Nature* **2018**, *556* (7699), 80−84.

(6) Jin, C.; Regan, E. C.; Yan, A.; Iqbal Bakti Utama, M.; Wang, D.; Zhao, S.; Qin, Y.; Yang, S.; Zheng, Z.; Shi, S. Observation of moiré excitons in WSe2/WS2 heterostructure superlattices. *Nature* **2019**, *567* (7746), 76−80.

(7) Tran, K.; Moody, G.; Wu, F.; Lu, X.; Choi, J.; Kim, K.; Rai, A.; Sanchez, D. A.; Quan, J.; Singh, A. Evidence for moiré excitons in van der Waals heterostructures. *Nature* **2019**, *567* (7746), 71−75.

(8) Alexeev, E. M.; Ruiz-Tijerina, D. A.; Danovich, M.; Hamer, M. J.; Terry, D. J.; Nayak, P. K.; Ahn, S.; Pak, S.; Lee, J.; Sohn, J. I. Resonantly hybridized excitons in moiré superlattices in van der Waals heterostructures. *Nature* **2019**, *567* (7746), 81−86.

(9) Regan, E. C.; Wang, D.; Jin, C.; Bakti Utama, M. I.; Gao, B.; Wei, X.; Zhao, S.; Zhao, W.; Zhang, Z.; Yumigeta, K. Mott and generalized Wigner crystal states in WSe2/WS2 moiré superlattices. *Nature* **2020**, *579* (7799), 359−363.

(10) Törmä, P.; Peotta, S.; Bernevig, B. A. Superconductivity, superfluidity and quantum geometry in twisted multilayer systems. *Nature Reviews Physics* **2022**, *4*, 528−542.

(11) Zhao, Y.; Zhang, C.; Kohler, D. D.; Scheeler, J. M.; Wright, J. C.; Voyles, P. M.; Jin, S. Supertwisted spirals of layered materials enabled by growth on non-Euclidean surfaces. *Science* **2020**, *370* (6515), 442−445.

(12) Zhao, Y.; Jin, S. Stacking and Twisting of Layered Materials Enabled by Screw Dislocations and Non-Euclidean Surfaces. *Acc. Mater. Res.* **2022**, *3* (3), 369−378.

(13) Zhang, X.; Tsai, K.-T.; Zhu, Z.; Ren, W.; Luo, Y.; Carr, S.; Luskin, M.; Kaxiras, E.; Wang, K. Correlated insulating states and transport signature of superconductivity in twisted trilayer graphene superlattices. *Phys. Rev. Lett.* **2021**, *127* (16), 166802.

(14) Zhu, Z.; Cazeaux, P.; Luskin, M.; Kaxiras, E. Modeling mechanical relaxation in incommensurate trilayer van der Waals heterostructures. *Phys. Rev. B* **2020**, *101* (22), 224107.

(15) Park, J. M.; Cao, Y.; Watanabe, K.; Taniguchi, T.; Jarillo-Herrero, P. Tunable strongly coupled superconductivity in magic-angle twisted trilayer graphene. *Nature* **2021**, *590* (7845), 249−255.

(16) Park, J. M.; Cao, Y.; Xia, L.-Q.; Sun, S.; Watanabe, K.; Taniguchi, T.; Jarillo-Herrero, P. Robust superconductivity in magic-angle multilayer graphene family. *Nat. Mater.* **2022**, *21*, 877−883.

(17) Xie, S.; Faeth, B. D.; Tang, Y.; Li, L.; Gerber, E.; Parzyck, C. T.; Chowdhury, D.; Zhang, Y.-H.; Jozwiak, C.; Bostwick, A. Strong interlayer interactions in bilayer and trilayer moiré superlattices. *Science advances* **2022**, *8* (12), eabk1911.

(18) Wu, F.; Zhang, R.-X.; Das Sarma, S. Three-dimensional topological twistronics. *Physical Review Research* **2020**, *2* (2), 022010.

(19) Khalaf, E.; Kruchkov, A. J.; Tarnopolsky, G.; Vishwanath, A. Magic angle hierarchy in twisted graphene multilayers. *Phys. Rev. B* **2019**, *100* (8), 085109.

(20) Zhang, W.; Hao, H.; Lee, Y.; Zhao, Y.; Tong, L.; Kim, K.; Liu, N. One-Interlayer-Twisted Multilayer MoS2Moiré Superlattices. *Adv. Funct. Mater.* **2022**, *32* (19), 2111529.

(21) Liu, F.; Wu, W.; Bai, Y.; Chae, S. H.; Li, Q.; Wang, J.; Hone, J.; Zhu, X.-Y. Disassembling 2D van der Waals crystals into macroscopic monolayers and reassembling into artificial lattices. *Science* **2020**, *367* (6480), 903−906.

(22) Meng, F.; Morin, S. A.; Forticaux, A.; Jin, S. Screw dislocation driven growth of nanomaterials. *Acc. Chem. Res.* **2013**, *46* (7), 1616−1626.

(23) Miller, D. L.; Kubista, K. D.; Rutter, G. M.; Ruan, M.; de Heer, W. A.; First, P. N.; Stroscio, J. A. Structural analysis of multilayer graphene via atomic moiré interferometry. *Phys. Rev. B* **2010**, *81* (12), 125427.

(24) Qiao, J.-B.; Yin, L.-J.; He, L. Twisted graphene bilayer around the first magic angle engineered by heterostrain. *Phys. Rev. B* **2018**, *98* (23), 235402.

(25) Wallbank, J. R.; Mucha-Kruczyński, M.; Chen, X.; Fal'Ko, V. I. Moiré superlattice effects in graphene/boron-nitride van der Waals heterostructures. *Ann. Phys. (Berlin, Ger.)* **2015**, *527* (5−6), 359−376.

(26) Cosma, D. A.; Wallbank, J. R.; Cheianov, V.; Fal'Ko, V. I. Moiré pattern as a magnifying glass for strain and dislocations in van der Waals heterostructures. *Faraday Discuss.* **2014**, *173*, 137−143.

(27) Jiang, Y.; Mao, J.; Duan, J.; Lai, X.; Watanabe, K.; Taniguchi, T.; Andrei, E. Y. Visualizing strain-induced pseudomagnetic fields in graphene through an hBN magnifying glass. *Nano Lett.* **2017**, *17* (5), 2839−2843.

(28) Shan, Y.; Li, Y.; Huang, D.; Tong, Q.; Yao, W.; Liu, W.-T.; Wu, S. Stacking symmetry governed second harmonic generation in graphene trilayers. *Science advances* **2018**, *4* (6), eaat0074.

(29) Sun, Z.; Yi, Y.; Song, T.; Clark, G.; Huang, B.; Shan, Y.; Wu, S.; Huang, D.; Gao, C.; Chen, Z. Giant nonreciprocal second-harmonic generation from antiferromagnetic bilayer CrI3. *Nature* **2019**, *572* (7770), 497−501.

(30) Li, Y.; Rao, Y.; Mak, K. F.; You, Y.; Wang, S.; Dean, C. R.; Heinz, T. F. Probing symmetry properties of few-layer MoS2 and h-BN by optical second-harmonic generation. *Nano Lett.* **2013**, *13* (7), 3329−3333.

(31) Mennel, L.; Furchi, M. M.; Wachter, S.; Paur, M.; Polyushkin, D. K.; Mueller, T. Optical imaging of strain in two-dimensional crystals. *Nat. Commun.* **2018**, *9*, 516.

(32) Liang, J.; Zhang, J.; Li, Z.; Hong, H.; Wang, J.; Zhang, Z.; Zhou, X.; Qiao, R.; Xu, J.; Gao, P. Monitoring local strain vector in atomic-layered MoSe2 by second-harmonic generation. *Nano Lett.* **2017**, *17* (12), 7539−7543.

(33) Hsu, W.-T.; Zhao, Z.-A.; Li, L.-J.; Chen, C.-H.; Chiu, M.-H.; Chang, P.-S.; Chou, Y.-C.; Chang, W.-H. Second harmonic generation from artificially stacked transition metal dichalcogenide twisted bilayers. *ACS Nano* **2014**, *8* (3), 2951−2958.

(34) Paradisanos, I.; Raven, A. M. S.; Amand, T.; Robert, C.; Renucci, P.; Watanabe, K.; Taniguchi, T.; Gerber, I. C.; Marie, X.; Urbaszek, B. Second harmonic generation control in twisted bilayers of transition metal dichalcogenides. *Phys. Rev. B* **2022**, *105* (11), 115420.

(35) Shearer, M. J.; Samad, L.; Zhang, Y.; Zhao, Y.; Puretzky, A.; Eliceiri, K. W.; Wright, J. C.; Hamers, R. J.; Jin, S. Complex and noncentrosymmetric stacking of layered metal dichalcogenide materials created by screw dislocations. *J. Am. Chem. Soc.* **2017**, *139* (9), 3496−3504.

(36) Fan, X.; Jiang, Y.; Zhuang, X.; Liu, H.; Xu, T.; Zheng, W.; Fan, P.; Li, H.; Wu, X.; Zhu, X. Broken symmetry induced strong nonlinear optical effects in spiral WS2 nanosheets. *ACS Nano* **2017**, *11* (5), 4892−4898.

(37) Zhang, L.; Liu, K.; Wong, A. B.; Kim, J.; Hong, X.; Liu, C.; Cao, T.; Louie, S. G.; Wang, F.; Yang, P. Three-dimensional spirals of atomic layered MoS2. *Nano Lett.* **2014**, *14* (11), 6418−6423.

(38) Khan, A. R.; Liu, B.; Lü, T.; Zhang, L.; Sharma, A.; Zhu, Y.; Ma, W.; Lu, Y. Direct measurement of folding angle and strain vector in atomically thin WS2 using second-harmonic generation. *ACS Nano* **2020**, *14* (11), 15806−15815.

(39) Qian, Q.; Zu, R.; Ji, Q.; Jung, G. S.; Zhang, K.; Zhang, Y.; Buehler, M. J.; Kong, J.; Gopalan, V.; Huang, S. Chirality-dependent second harmonic generation of MoS2 nanoscroll with enhanced efficiency. *ACS Nano* **2020**, *14* (10), 13333−13342.

(40) Psilodimitrakopoulos, S.; Mouchliadis, L.; Paradisanos, I.; Kourmoulakis, G.; Lemonis, A.; Kioseoglou, G.; Stratakis, E. Twist angle mapping in layered WS2 by polarization-resolved second harmonic generation. *Sci. Rep.* **2019**, *9*, 14285.

(41) Psilodimitrakopoulos, S.; Orekhov, A.; Mouchliadis, L.; Jannis, D.; Maragkakis, G.; Kourmoulakis, G.; Gauquelin, N.; Kioseoglou, G.; Verbeeck, J.; Stratakis, E. Optical versus electron diffraction imaging of Twist-angle in 2D transition metal dichalcogenide bilayers. *npj 2D Mater. Appl.* **2021**, *5*, 77.

(42) Zhao, M.; Ye, Z.; Suzuki, R.; Ye, Y.; Zhu, H.; Xiao, J.; Wang, Y.; Iwasa, Y.; Zhang, X. Atomically phase-matched second-harmonic generation in a 2D crystal. *Light: Science & Applications* **2016**, *5* (8), e16131−e16131.

(43) Berkdemir, A.; Gutiérrez, H. R.; Botello-Méndez, A. R.; Perea-López, N.; Elías, A. L.; Chia, C.-I.; Wang, B.; Crespi, V. H.; López-Urías, F.; Charlier, J.-C. Identification of individual and few layers of WS2 using Raman Spectroscopy. *Sci. Rep.* **2013**, *3*, 1755.

(44) Conley, H. J.; Wang, B.; Ziegler, J. I.; Haglund, R. F., Jr; Pantelides, S. T.; Bolotin, K. I. Bandgap engineering of strained monolayer and bilayer MoS2. *Nano Lett.* **2013**, *13* (8), 3626−3630.

(45) Wang, F.; Kinloch, I. A.; Wolverson, D.; Tenne, R.; Zak, A.; O'Connell, E.; Bangert, U.; Young, R. J. Strain-induced phonon shifts in tungsten disulfide nanoplatelets and nanotubes. *2D Materials* **2017**, *4* (1), 015007.

(46) Liu, K.; Zhang, L.; Cao, T.; Jin, C.; Qiu, D.; Zhou, Q.; Zettl, A.; Yang, P.; Louie, S. G.; Wang, F. Evolution of interlayer coupling in twisted molybdenum disulfide bilayers. *Nat. Commun.* **2014**, *5*, 4966.

(47) Li, D.; Wei, C.; Song, J.; Huang, X.; Wang, F.; Liu, K.; Xiong, W.; Hong, X.; Cui, B.; Feng, A. Anisotropic enhancement of second-harmonic generation in monolayer and bilayer MoS2 by integrating with TiO2 nanowires. *Nano Lett.* **2019**, *19* (6), 4195−4204.

(48) Huder, L.; Artaud, A.; Le Quang, T.; De Laissardiere, G. T.; Jansen, A. G.; Lapertot, G.; Chapelier, C.; Renard, V. T. Electronic spectrum of twisted graphene layers under heterostrain. *Phys. Rev. Lett.* **2018**, *120* (15), 156405.

(49) Bai, Y.; Zhou, L.; Wang, J.; Wu, W.; McGilly, L. J.; Halbertal, D.; Lo, C. F. B.; Liu, F.; Ardelean, J.; Rivera, P. Excitons in strain-induced one-dimensional moiré potentials at transition metal dichalcogenide heterojunctions. *Nat. Mater.* **2020**, *19* (10), 1068−1073.

(50) Edelberg, D.; Kumar, H.; Shenoy, V.; Ochoa, H.; Pasupathy, A. N. Tunable strain soliton networks confine electrons in van der Waals materials. *Nat. Phys.* **2020**, *16* (11), 1097−1102.

(51) Mesple, F.; Missaoui, A.; Cea, T.; Huder, L.; Guinea, F.; de Laissardière, G. T.; Chapelier, C.; Renard, V. T. Heterostrain determines flat bands in magic-angle twisted graphene layers. *Phys. Rev. Lett.* **2021**, *127* (12), 126405.

(52) Bi, Z.; Yuan, N. F.; Fu, L. Designing flat bands by strain. *Phys. Rev. B* **2019**, *100* (3), 035448.

(53) Klein, J.; Wierzbowski, J.; Steinhoff, A.; Florian, M.; Rosner, M.; Heimbach, F.; Muller, K.; Jahnke, F.; Wehling, T. O.; Finley, J. J. Electric-field switchable second-harmonic generation in bilayer MoS2 by inversion symmetry breaking. *Nano Lett.* **2017**, *17* (1), 392−398.

(54) Zhang, M.; Han, N.; Wang, J.; Zhang, Z.; Liu, K.; Sun, Z.; Zhao, J.; Gan, X. Strong Second Harmonic Generation from Bilayer Graphene with Symmetry Breaking by Redox-Governed Charge Doping. *Nano Lett.* **2022**, *22* (11), 4287−4293.

(55) Wang, K.; Puretzky, A. A.; Hu, Z.; Srijanto, B. R.; Li, X.; Gupta, N.; Yu, H.; Tian, M.; Mahjouri-Samani, M.; Gao, X. Strain tolerance of two-dimensional crystal growth on curved surfaces. *Science advances* **2019**, *5* (5), eaav4028.

(56) Liao, M.; Nicolini, P.; Du, L.; Yuan, J.; Wang, S.; Yu, H.; Tang, J.; Cheng, P.; Watanabe, K.; Taniguchi, T. UItra-low friction and edge-pinning effect in large-lattice-mismatch van der Waals heterostructures. *Nat. Mater.* **2022**, *21* (1), 47−53.

(57) Zhu, Z.; Carr, S.; Massatt, D.; Luskin, M.; Kaxiras, E. Twisted trilayer graphene: A precisely tunable platform for correlated electrons. *Phys. Rev. Lett.* **2020**, *125* (11), 116404.

(58) Ci, P.; Chen, Y.; Kang, J.; Suzuki, R.; Choe, H. S.; Suh, J.; Ko, C.; Park, T.; Shen, K.; Iwasa, Y. Quantifying van der Waals interactions in layered transition metal dichalcogenides from pressure-enhanced valence band splitting. *Nano Lett.* **2017**, *17* (8), 4982−4988.

(59) Ci, P.; Tian, X.; Kang, J.; Salazar, A.; Eriguchi, K.; Warkander, S.; Tang, K.; Liu, J.; Chen, Y.; Tongay, S.; Walukiewicz, W.; Miao, J.; Dubon, O.; Wu, J. Chemical trends of deep levels in van der Waals semiconductors. *Nat. Commun.* **2020**, *11* (1), 5373.

(60) Lu, F.; Sun, Z.; Wu, S.; Liu, W.-T. Bond additivity model for anisotropic second-harmonic generation from two-dimensional honeycomb lattices. *Opt. Lett.* **2020**, *45* (2), 268−271.

(61) Xia, H.; Chen, X.; Luo, S.; Qin, F.; Idelevich, A.; Ghosh, S.; Ideue, T.; Iwasa, Y.; Zak, A.; Tenne, R. Probing the chiral domains and excitonic states in individual WS2 tubes by second-harmonic generation. *Nano Lett.* **2021**, *21* (12), 4937−4943.

(62) Xia, F.; Wang, H.; Hwang, J.; Neto, A.; Yang, L. Black phosphorus and its isoelectronic materials. *Nature Reviews Physics* **2019**, *1* (5), 306−317.

(63) Zhang, Y.; Ideue, T.; Onga, M.; Qin, F.; Suzuki, R.; Zak, A.; Tenne, R.; Smet, J.; Iwasa, Y. Enhanced intrinsic photovoltaic effect in tungsten disulfide nanotubes. *Nature* **2019**, *570* (7761), 349−353.

(64) Son, J.; Kim, K.-H.; Ahn, Y.; Lee, H.-W.; Lee, J. Strain engineering of the Berry curvature dipole and valley magnetization in monolayer MoS 2. *Phys. Rev. Lett.* **2019**, *123* (3), 036806.

(65) Lee, J.; Wang, Z.; Xie, H.; Mak, K. F.; Shan, J. Valley magnetoelectricity in single-layer MoS2. *Nat. Mater.* **2017**, *16* (9), 887−891.

(66) Ma, Q.; Xu, S.-Y.; Shen, H.; MacNeill, D.; Fatemi, V.; Chang, T.-R.; Mier Valdivia, A. M.; Wu, S.; Du, Z.; Hsu, C.-H. Observation of

the nonlinear Hall effect under time-reversal-symmetric conditions. *Nature* **2019**, *565* (7739), 337−342.

(67) Sodemann, I.; Fu, L. Quantum nonlinear Hall effect induced by Berry curvature dipole in time-reversal invariant materials. *Phys. Rev. Lett.* **2015**, *115* (21), 216806.

📖 Recommended by ACS

Photoinduced Rippling of Two-Dimensional Hexagonal Nitride Monolayers

Kun Liu, Jian Zhou, *et al.*

NOVEMBER 07, 2022
NANO LETTERS   READ 🗗

Flake Size Limits for Growth of Vertically Stacked Two-Dimensional Materials by Analytical Diffusion-Based Kinetic Model

Han Ye, Zhenlin Guo, *et al.*

AUGUST 29, 2022
CRYSTAL GROWTH & DESIGN   READ 🗗

Moiré Modulation of Van Der Waals Potential in Twisted Hexagonal Boron Nitride

Stefano Chiodini, Antonio Ambrosio, *et al.*

APRIL 29, 2022
ACS NANO   READ 🗗

Are 2D Interfaces Really Flat?

Zhihui Cheng, Curt A. Richter, *et al.*

MARCH 15, 2022
ACS NANO   READ 🗗

Get More Suggestions >

Supporting Information

Breaking rotational symmetry in supertwisted WS₂ spirals via moiré magnification of intrinsic heterostrain

Penghong Ci,[1,2,3,+] Yuzhou Zhao,[4,+] Muhua Sun,[5,+] Yoonsoo Rho,[6,7] Yabin Chen,[8] Costas P. Grigoropoulos,[6] Song Jin,[4] Xiaoguang Li,[3,*] Junqiao Wu[1,2,*]

[1] Department of Materials Science and Engineering, University of California, Berkeley, California 94720, United States

[2] Materials Sciences Division, Lawrence Berkeley National Laboratory, Berkeley, California 94720, United States

[3] Institute for Advanced Study, Shenzhen University, Shenzhen 518060, China

[4] Department of Chemistry, University of Wisconsin–Madison, Madison, WI 53706, United States

[5] National Center for Electron Microscopy in Beijing, School of Materials Science and Engineering, Tsinghua University, Beijing 100084, China

[6] Department of Mechanical Engineering, University of California, Berkeley, California 94720, United States

[7] Physical & Life Sciences and NIF & Photon Sciences, Lawrence Livermore National Laboratory, Livermore, California 94550, United States

[8] School of Aerospace Engineering, Beijing Institute of Technology, Beijing, China

[*] E-mail: wuj@berkeley.edu, xgli@szu.edu.cn

Methods.

Synthesis of WS₂ nanostructures. The WS$_2$ spiral structures were synthesized following previous reports.[1, 2] WO$_3$ nanoparticles (Sigma Aldrich, nanopowder, <100 nm particle size) dispersed in ethanol were drop cast onto a 300 nm SiO$_2$/Si substrate and dried prior to the reaction. 100 mg WS$_2$ precursor powder (Alfa Aesar) in an alumina boat was placed in the first zone of a three-zone furnace. The substrates were placed between the second and the third zone with the polished side facing up. 1 g CaSO$_4$·2H$_2$O powder (Sigma Aldrich) was placed upstream from the heating zone as the water vapor source and heated with heating tapes. With 100 sccm argon flowing at 800 torr, the second zone was heated to 1200 °C at a rate of 20 °C/min, and simultaneously the third zone was heated to 700 °C at the same rate, while the CaSO$_4$·2H$_2$O was not heated. Once the furnace temperatures were reached, the CaSO$_4$·2H$_2$O was heated to 90 °C to release the water vapor. After all the temperatures were stabilized, the WS$_2$ boat was pushed into the second zone by a magnet coupled positioner and a quartz rod to initiate the reaction. After 15 min reaction, the furnace was opened and cooled down rapidly.

Polarization resolved second harmonic generation (SHG) intensity patterns and imaging. SHG measurement was performed using a Ti:Sapphire femtosecond laser with ~800 nm of wavelength, ~100fs of pulse width, and 80 MHz of repetition rate. The laser beam was mechanically chopped for signal demodulation to suppress the background noise. The polarization of the input laser beam was controlled by a half-wave plate and focused through a 50X long working distance objective lens. The generated SHG signal at ~400 nm was collected through the same objective lens and separated from the input fundamental laser beam by a harmonic separator. A polarizer filtered the polarization of the SHG signal, and color filters were used to block the fundamental laser beam. A photomultiplier tube (PMT) collected the SHG signal, which was demodulated at the modulation of the frequency of the input laser beam by a lock-in amplifier.

Density-functional theory (DFT) calculations. DFT calculations were performed using Vienna ab initio simulation package with projector-augmented wave pseudopotentials.[3, 4] The generalized gradient approximation of Perdew−Burke−Ernzerhof was used for the exchange-correlation functionals.[5] The cutoff energy for the plane-wave basis was set to 450 eV. The convergence criteria of energy and forces were set to 1×10^{-4} eV and 0.05 eV Å^{-1}, respectively. The van der Waals interaction was induced by using the D3 correction scheme of Grimme.[6] For charge density difference calculations in twisted bilayer WS$_2$, we explored 4×4 supercell as discussed in previous studies.[7, 8] The bottom pristine monolayer WS$_2$ with D_{3h} symmetry has zigzag crystal orientation aligned with x-axis; the top layer with ~3% strain is twisted clockwise by ~7º with respect to the bottom layer. The 4×4 grid of unstrained WS$_2$ primitive cell was combined with the corresponding size strained WS$_2$ to build the supercell of homostructure and allow relaxation for DFT calculations. The k-point sampling was obtained from the Monkhorst−Pack scheme with a 4×4×1 mesh.

Raman and AFM characterization. Raman spectra were measured by a Raman spectrometer (Renishaw Inc.) with a 488 nm laser as the excitation source. Sample morphology was characterized by an AFM system (Vistascope, Molecular Vista) in the tapping mode.
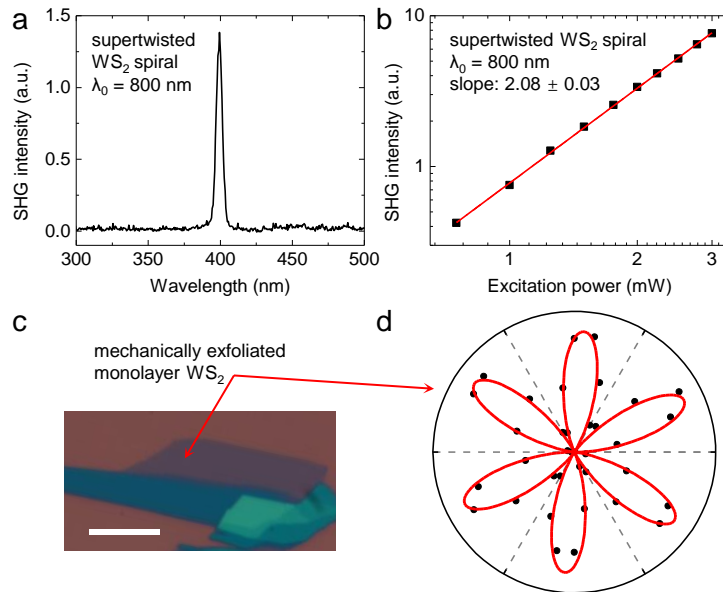
Figure S1. SHG response of the supertwisted WS$_2$ spiral and monolayer WS$_2$. (a) & (b) SHG signal intensity as a function of photon energy and excitation laser ($\lambda_0(\omega)$ = 800 nm) power in supertwisted WS$_2$ spiral. The SHG feature appears at the wavelength 400 nm (2ω), and its intensity grows quadratically with the incident power, verified by the slope of the fitted solid line to be 2.08 ±0.03. (c) & (d) Optical microscopy of mechanically exfoliated monolayer WS$_2$ (scale bar: 10 μm) and its polarization resolved SHG intensity pattern. Symbols are experimental data; curves are fitted via $I \propto |cos3\phi|^2$ (see details in the main text).
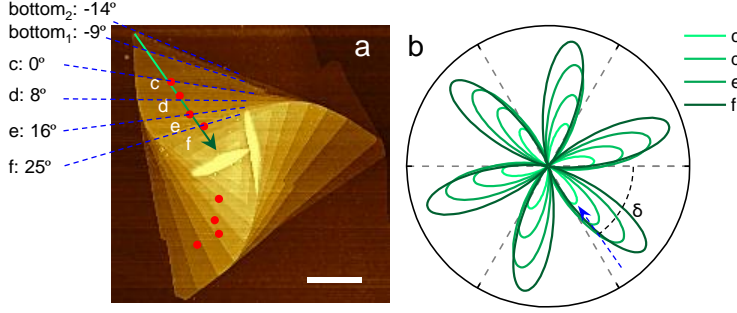
Figure S2. Simulations of SHG patterns in the supertwisted WS₂ spiral based on SH field superposition theory considering the material absorption. (a) AFM mapping image of the supertwisted spiral (scale bar: 1 μm), where the twist angles relative to the layer "c" are labeled. (b) Calculated SHG patterns in positions of "c" – "f" by SH field superposition theory show six-fold SHG patterns and thus cannot explain the experimental results in Figure 1. The blue arrow indicates the average "armchair" orientations (δ) at the position of "c".

Based on the SH field superposition theory, for stacked bilayers with a twisting angle θ, the total SH field ($\vec{E}_{2\omega}^T$) is the vector addition of dipole moments ($\vec{E}_{2\omega}^1$ and $\vec{E}_{2\omega}^2$) from two electrically decoupled layers: $\vec{E}_{2\omega}^T = \vec{E}_{2\omega}^1 + \vec{E}_{2\omega}^2 \propto cos3\phi + cos3(\phi + \theta)$.[9] 2H stacked bilayers ($\theta = 60°$) yield a completely destructive interference of SH fields ($\vec{E}_{2\omega}^T = 0$), whereas $\theta = 0°$, corresponding to the 3R-like stacking, yields a constructive superposition of SH fields. Hence the SHG intensity increases with the increasing number of 3R-like stacked layers,[10] explaining the enhancement of SHG intensity toward the center of the aligned spiral (Figure 2c).

When considering the material absorption, the SH field from the Nth layer can be written as:[10]

$$\vec{E}_{2\omega}^N \propto \Gamma_N cos\ 3(\phi - \delta_N)\ \text{(S1)}$$

where $\Gamma_N = e^{i\Delta k(N-1)t}e^{-\alpha(N-1)t/2}$ defines the attenuation factor of the SH field from the Nth layer due to the material absorption, ϕ is the azimuthal angle between the armchair direction and the incident laser polarization direction, α means absorption coefficient of WS₂ to be 0.086 nm⁻¹ at 400 nm,[11] t is the thickness between the surface and the Nth layer of the sample, δ_N is the twisting angle of the Nth layer relative to the layer "c" denoted in the left of Figure S2a, $\Delta k = \frac{4\pi}{\lambda_0(\omega)}(-n(2\omega) - n(\omega))$ is the wave-vector difference between the fundamental (ω) and the SH (2ω) light, λ_0 is the wavelength of the fundamental laser to be 800 nm, $n(2\omega)$ and $n(\omega)$ mean the refractive index of WS₂ to be 3.78 at 400 nm and 4.10 at 800 nm,[12] respectively. According to the SH field superposition theory, the total SH field ($\vec{E}_{2\omega}^{Total}$) is the vector additions of dipole moments from each electrically decoupled individual layer ($\vec{E}_{2\omega}^N$):

$$\vec{E}_{2\omega}^{Total}(N, \delta) \propto \sum_{M=1}^{N} \Gamma_M cos\ 3(\phi - \delta_M).\ \text{(S2)}$$

Thus, the total SHG ($I_{2\omega}^{Total} \propto \left|\vec{E}_{2\omega}^{Total}\right|^2$) at different positions were calculated in Figure S2b. These patterns show full six-fold symmetry, indicating that the traditional SH field superposition theory cannot explain the experimental two-lobe SHG patterns in the supertwisted spiral (Figure 1). The average "armchair" orientations of δ fitted by SH field

superposition theory are consistent with those fitted by the modified bond additivity model in Figure 5b.
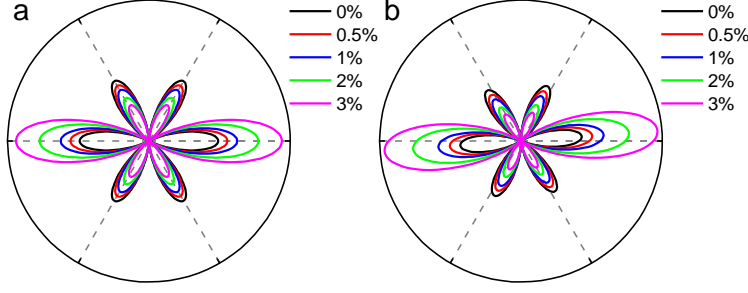
Figure S3. Simulations of SHG patterns in WS₂ under strain. (a) Calculated SHG patterns in monolayer WS₂ under various strains by Mennel's model. (b) Calculated SHG patterns in the supertwisted WS₂ spiral with the structure in Figure S2a as a function of strain, using a model based on a combination of Mennel's equation (eq S3), SH superposition theory, and the material absorption.

Mennel et al. demonstrated that SHG intensity patterns of monolayer TMDs under uniaxial strain are

$$I \propto \frac{1}{4}\left(A cos3\phi + B cos(2\phi + \gamma)\right)^2 \text{ (S3)}$$

with $A = (1-\nu)(p_1 + p_2)(\varepsilon_{xx} + \varepsilon_{yy}) + 2\chi_0$ and $B = (1+\nu)(p_1 - p_2)(\varepsilon_{xx} - \varepsilon_{yy})$.[13] For WS₂, p_1 and p_2 are photoelastic parameters to be 0.75 and -0.97 nm/V/%, ε_{xx} and ε_{yy} are principal strains, χ_0 is the nonlinear susceptibility parameter of the unstrained crystal lattice to be 7.5 nm/V, ν is the Poisson ratio to be 0.22, ϕ is the polarization angle, γ denotes the principal strain orientation.[14] When setting $\gamma = 0°$ and $\varepsilon_{yy} = 0$, we calculated SHG patterns of monolayer WS₂ as a function of various ε_{xx} in Figure S3a. Considering the absorption-induced attenuation factor (Γ_N) of the SH field from the Nth layer, we combined eqs S1-S3 to obtain the SHG intensity formula for the supertwisted spiral under uniform strain

$$I \propto \left| \sum_{M=1}^{N} \Gamma_M [A cos3(\phi - \delta_M) + B cos(2(\phi-\delta_M) + \gamma)] \right|^2. \text{ (S4)}$$

Figure S3b shows SHG patterns of the supertwisted spiral with the structure in Figure S2a under uniform ε_{xx} strain ($\gamma = 0°$, $\varepsilon_{yy} = 0$), which are inconsistent with experimental two-lobe SHG patterns in Figure 1.
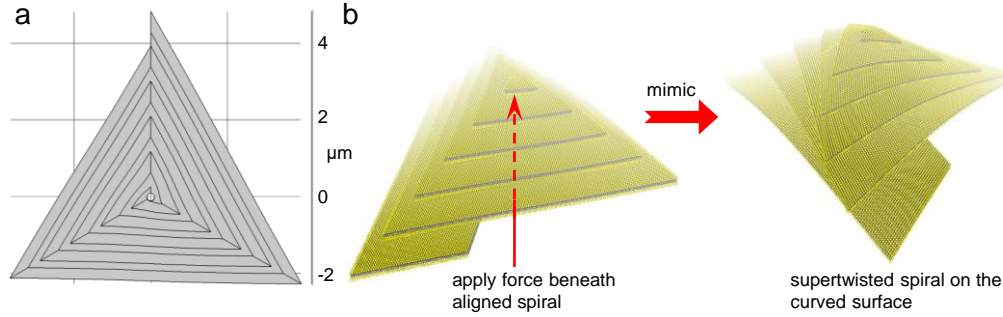
Figure S4. COMSOL multiphysics simulations. (a) COMSOL model of the spiral structure. (b) Sketch of a Euclidean aligned spiral and a non-Euclidean supertwisted spiral.

We determined the existence of heterostrain between adjacent layers in the supertwisted spiral structure using steady-state finite-element method (FEM) calculations (COMOSOL multiphysics with the Solid Mechanics module). Due to the challenge of building a supertwisted geometry above the curved surface, the regular spiral model was created in Figure S4a. An out-of-plane force was applied beneath the center of the aligned spiral to qualitatively mimic the influence of protrusion on the formation of the supertwisted spiral in Figure S4b, based on the mechanism of the "non-Euclidean" twist in our previous publication.[2] We note that as a result of the spiral shape in the three-dimensional space, its parallel cross section is not a complete triangle but a concave quadrilateral shape, as shown in Figure 4b. When applying the out-of-plane force beneath the spiral, the deformation increases from the upper layer to the lower layer (Figure 4b), suggesting the presence of heterostrain in the supertwisted spiral.

We note that the FEM simulations only qualitatively demonstrated the presence of distinct tensile strain among neighboring layers in the supertwisted structure, because real strain values in each layer are largely defined by the size of the protrusion and the relaxation process during the sample synthesis, which is challenging to be accurately simulated by COMSOL. However, real values of heterostrains in the supertwisted spirals do not affect the main conclusion of our work because a small heterostrain can be magnified about 10-fold, thus significantly distorting the moiré pattern and breaking the overall symmetry, as shown in Figure 4d.
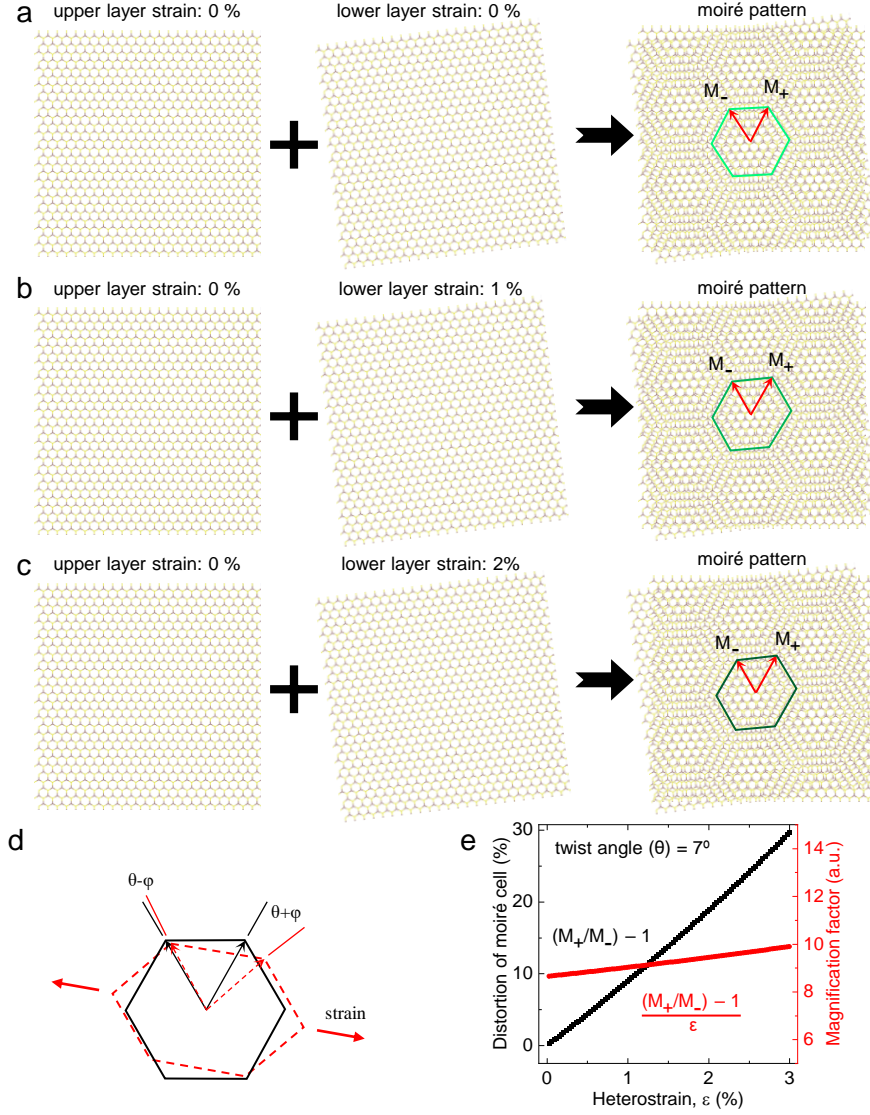
Figure S5. Symmetry transition induced by moiré magnification of heterostrain in twisted TMD bilayers. (a)-(c) The upper layer is unstrained, but the lower layer undergoes different strains of 0%, 1%, and 2%, hence forming moiré patterns with different shapes (twist angle of 7º). (d) Strained and rotated unit cell of the lower layer (dashed line) with respect to unstrained unit cell (solid line) in the upper layer.[15, 16] (e) Length distortion ($M+/M-$ − 1) between two vectors of the moiré supercell and the magnification factor (($M+/M-$ − 1)/ε) as a function of relative strain (ε) between neighboring twisted layers.

The two vectors of the moiré supercell in Figures S5a-c are modulated by heterostrain to be

$$M_{\pm} = \frac{a(1+\epsilon_{\pm})}{2\sqrt{(1+\epsilon_{\pm})\sin^2{[(\theta+\varphi_{\pm})/2]}+\epsilon_{\pm}^2/4}}. \text{[15, 16] (S5)}$$

For WS$_2$, the in-plane unit cell parameter is 0.315 nm; under a small strain approximation (ε << 1), we get $\epsilon_{\pm} \approx \frac{1}{4}(1-3\nu)\varepsilon$ and $\varphi_{\pm} \approx \pm\sqrt{3}\varepsilon|\frac{1+\nu}{4+\varepsilon(1-3\nu)}|$,[15, 16] where the Poisson ratio (ν) is 0.22.[14] The twist angle (θ) is tailored to $\theta + \varphi_{\pm}$ along two lattice vectors by heterostrain in Figure S5d.

8

When both layers have the same strain magnitude, the moiré pattern presents a regular hexagon shape, marked by the light green color in (a). The regular hexagonal moiré pattern is distorted into elongated hexagons for twisted TMD bilayers under heterostrain in (b)-(c).

Note S1. Eliminating the impact of oblique incidence on the SHG response.

The polarization resolved SHG patterns in Figure 1 were measured at positions away from the protrusion beneath the supertwisted spirals to ensure the normal incidence. Furthermore, due to the large ratio between the width (~200 nm) and the height (~0.7 nm) of the step, the stair angle of the spiral is too small to affect the SHG patterns. It has been reported that when the incident angle of the fundamental laser is η, the SHG intensity can be expressed as $I \propto |cos^2\eta \cdot cos3\phi|^2$.[17, 18] Thus, in our spiral structure, the η value is so small (<< 1º) that the influence of oblique incidence on SHG is negligible.

Note S2. Modified bond additivity model to fit SHG patterns of the supertwisted spiral.

The polarization dependent SHG signal can be evaluated by the bond additivity mode (BAM).[19] Here, we consider a phenomenological mode by adding an effective bond to introduce the observed asymmetric two-fold signal in the SHG pattern.

The twist in the spiral structure will not affect the D_{3h} symmetry of each WS_2 layer, so the 6-fold symmetry of the SHG pattern was initially expected to be preserved. However, our SHG signal exhibits a stronger angular preference closer to the center of the supertwisted spiral, where the heterostrain between neighboring twisted layers is enhanced. Based on the bond additivity model, the asymmetric phenomena can be explained by introducing an effective bond to describe the moiré magnification of heterostrain and the resultant elongated hexagon moiré patterns in Figures 5d and S5.

We assume the incident polarized light with the electric field as

$$\boldsymbol{E} = E_0 \hat{e} = E_0(\sin\phi, \cos\phi, 0)^T$$

where ϕ is the angle between incident laser polarization and the y-axis of the lab coordinate, as shown in Figure 5a. For the WS_2 layer with D_{3h} symmetry, the SHG comes from three effective linear bonds. Each of these bonds has the only nonzero hyperpolarizability tensor element $\beta_{yyy}^{(2)} = \beta_0$, where y indicates the direction along this bond. Moreover, we consider an additional effective bond with an angle α relative to y-axis of the lab coordinate, and its $\beta_{yyy}^{(2)} = \beta_0 \rho e^{i\Theta}$. Now, in the lab coordinate, we have the total hyperpolarizability tensor

$$\beta_{lmn}^{(2)} = \beta_0 \rho e^{i\Theta}(\hat{l}\cdot\hat{\rho})(\hat{m}\cdot\hat{\rho})(\hat{n}\cdot\hat{\rho}) + \sum_i \sum_{lmn} \beta_{lmn}^{(2),i}(\hat{x}\cdot\hat{l})(\hat{x}\cdot\hat{m})(\hat{y}\cdot\hat{n})$$

where $\hat{\rho} = (\sin\alpha, \cos\alpha, 0)^T$ is the direction of the additional bond in the lab coordinate, i stands for the different WS_2 bonds within the D_{3h} symmetry bond, and lmn indicate the bond coordinate. We note that the z component of the effective bonds will not affect the SHG result.

The SHG intensity can be calculated as

$$P_i(2\omega) = \epsilon_0 \sum_{jk} \chi_{ijk}^{(2)} E_j E_k = \epsilon_0 \sum_{jk} 2d_{ijk} E_j E_k$$

$$I_{SHG}(\phi) = \left| \epsilon_0 \sum_{ijk} E_i(2\omega)\chi_{ijk}^{(2)} E_j(\omega) E_k(\omega) \right|^2 = \left| \epsilon_0 \sum_{ijk} E_i(2\omega)2d_{ijk} E_j(\omega) E_k(\omega) \right|^2$$

$$d = \begin{bmatrix} \chi_{xxx} & \chi_{xyy} & \chi_{xzz} & \chi_{xyz} & \chi_{xzx} & \chi_{xxy} \\ \chi_{yxx} & \chi_{yyy} & \chi_{yzz} & \chi_{yyz} & \chi_{yzx} & \chi_{yxy} \\ \chi_{zxx} & \chi_{zyy} & \chi_{zzz} & \chi_{zyz} & \chi_{zzx} & \chi_{zxy} \end{bmatrix} \begin{bmatrix} \sin^2\phi \\ \cos^2\phi \\ 0 \\ 0 \\ 0 \\ 2\sin\phi\cos\phi \end{bmatrix}$$

For the above incident field, we can write the nonlinear susceptibility tensor as

$$d = \begin{bmatrix} \chi_{xxx} & \chi_{xyy} & 0 & 0 & 0 & \chi_{xxy} \\ \chi_{yxx} & \chi_{yyy} & 0 & 0 & 0 & \chi_{yxy} \\ 0 & 0 & 0 & 0 & 0 & 0 \end{bmatrix}$$

The WS_2 bonds are

11

$$\rho_1 = (0,1,0)^T$$

$$\rho_2 = \left(\sqrt{3}/2, -1/2, 0\right)^T$$

$$\rho_3 = \left(-\sqrt{3}/2, -1/2, 0\right)^T$$

We can obtain

$$\beta_{xxy}^{(2)} = \sum_i \sum_{lmn} \beta_{lmn}^{(i)}(\hat{x} \cdot \hat{l})(\hat{x} \cdot \hat{m})(\hat{y} \cdot \hat{n}) + \rho(\hat{x} \cdot \hat{\rho})(\hat{x} \cdot \hat{\rho})(\hat{x} \cdot \hat{\rho})$$

$$= \left[\rho e^{i\Theta} \sin^2 \alpha \cos \alpha - \frac{3}{4}\right]\beta_0$$

Similarly, we have

$$\beta_{xxx}^{(2)} = \rho e^{i\Theta} \sin^3 \alpha \ \beta_0$$

$$\beta_{yxx}^{(2)} = \beta_{xxy}^{(2)} = \left[\rho e^{i\Theta} \sin^2 \alpha \cos \alpha - \frac{3}{4}\right]\beta_0$$

$$\beta_{xyy}^{(2)} = \beta_{yxy}^{(2)} = \rho(\hat{x} \cdot \hat{\rho})(\hat{y} \cdot \hat{\rho})(\hat{y} \cdot \hat{\rho}) = \rho e^{i\Theta} \sin \alpha \ \cos^2 \alpha \ \beta_0$$

$$\beta_{yyy}^{(2)} = \rho(\hat{y} \cdot \hat{\rho})(\hat{y} \cdot \hat{\rho})(\hat{y} \cdot \hat{\rho}) = \left[\rho e^{i\Theta} \cos^3 \alpha + \frac{3}{4}\right]\beta_0$$

Finally, we obtain

$$I_{SHG}(\theta) = N\beta_0^2 \left|\rho e^{i\Theta} \cos^3(\alpha - \phi) + \frac{3}{4}\cos 3\phi\right|^2. \quad (S6)$$

where N is the number of atoms participating in the SH response. Close to the center region, the easy deformation nature and the overall C$_3$ rotational symmetry breaking response to the second harmonic measurement.

Table I: Fitted parameters of SHG patterns for different positions in the supertwisted spiral (Figure 1a).

	δ (°)	δ+α (°)	ρ (a.u.)	Θ (°)
c	-54.9	-30	0	1
d	-52.5	-40.3	0.62	95.4
e	-48.9	-45.2	1.06	105.7
f	-45.8	-45.9	2.2	130.2

REFERENCES

1. Zhao, Y.; Jin, S. Controllable water vapor assisted chemical vapor transport synthesis of WS2–MoS2 heterostructure. *ACS Materials Letters* **2020,** 2, (1), 42-48.

2. Zhao, Y.; Zhang, C.; Kohler, D. D.; Scheeler, J. M.; Wright, J. C.; Voyles, P. M.; Jin, S. Supertwisted spirals of layered materials enabled by growth on non-Euclidean surfaces. *Science* **2020,** 370, (6515), 442-445.

3. Kresse, G.; Furthmüller, J. Efficient iterative schemes for ab initio total-energy calculations using a plane-wave basis set. *Physical review B* **1996,** 54, (16), 11169.

4. Blöchl, P. E. Projector augmented-wave method. *Physical review B* **1994,** 50, (24), 17953.

5. Perdew, J. P.; Burke, K.; Ernzerhof, M. Generalized gradient approximation made simple. *Phys. Rev. Lett.* **1996,** 77, (18), 3865.

6. Grimme, S.; Antony, J.; Ehrlich, S.; Krieg, H. A consistent and accurate ab initio parametrization of density functional dispersion correction (DFT-D) for the 94 elements H-Pu. *The Journal of chemical physics* **2010,** 132, (15), 154104.

7. Zhu, Z.; Cazeaux, P.; Luskin, M.; Kaxiras, E. Modeling mechanical relaxation in incommensurate trilayer van der Waals heterostructures. *Physical Review B* **2020,** 101, (22), 224107.

8. Naik, M. H.; Jain, M. Ultraflatbands and shear solitons in moiré patterns of twisted bilayer transition metal dichalcogenides. *Phys. Rev. Lett.* **2018,** 121, (26), 266401.

9. Hsu, W.-T.; Zhao, Z.-A.; Li, L.-J.; Chen, C.-H.; Chiu, M.-H.; Chang, P.-S.; Chou, Y.-C.; Chang, W.-H. Second harmonic generation from artificially stacked transition metal dichalcogenide twisted bilayers. *ACS nano* **2014,** 8, (3), 2951-2958.

10. Zhao, M.; Ye, Z.; Suzuki, R.; Ye, Y.; Zhu, H.; Xiao, J.; Wang, Y.; Iwasa, Y.; Zhang, X. Atomically phase-matched second-harmonic generation in a 2D crystal. *Light: Science & Applications* **2016,** 5, (8), e16131-e16131.

11. Hsu, C.; Frisenda, R.; Schmidt, R.; Arora, A.; De Vasconcellos, S. M.; Bratschitsch, R.; van der Zant, H. S.; Castellanos-Gomez, A. Thickness-dependent refractive index of 1L, 2L, and 3L MoS2, MoSe2, WS2, and WSe2. *Advanced optical materials* **2019,** 7, (13), 1900239.

12. Jung, G.-H.; Yoo, S.; Park, Q.-H. Measuring the optical permittivity of two-dimensional materials without a priori knowledge of electronic transitions. *Nanophotonics* **2019,** 8, (2), 263-270.

13. Mennel, L.; Furchi, M. M.; Wachter, S.; Paur, M.; Polyushkin, D. K.; Mueller, T. Optical imaging of strain in two-dimensional crystals. *Nature communications* **2018,** 9, 516.

14. Mennel, L.; Paur, M.; Mueller, T. Second harmonic generation in strained transition metal dichalcogenide monolayers: MoS2, MoSe2, WS2, and WSe2. *APL Photonics* **2019,** 4, (3), 034404.

15. Miller, D. L.; Kubista, K. D.; Rutter, G. M.; Ruan, M.; de Heer, W. A.; First, P. N.; Stroscio, J. A. Structural analysis of multilayer graphene via atomic moiré interferometry. *Physical Review B* **2010,** 81, (12), 125427.

16. Qiao, J.-B.; Yin, L.-J.; He, L. Twisted graphene bilayer around the first magic angle engineered by heterostrain. *Physical Review B* **2018,** 98, (23), 235402.

17. He, C.; Wu, R.; Qi, M.; Huang, Y.; Zhou, Y.; Zhang, S.; Zhao, Q.; Xu, X. Dispersion Property and Evolution of Second Harmonic Generation Pattern in Type-I and Type-II van der Waals Heterostructures. *ACS Applied Materials & Interfaces* **2021,** 13, (23), 27334-27342.

18. He, C.; Zhu, L.; Huang, Y.; Du, W.; Qi, M.; Zhou, Y.; Zhao, Q.; Xu, X. Accurately Controlling Angle-Resolved Second Harmonic Generation by Stacking Orders from a MoS2 Homobilayer. *The Journal of Physical Chemistry C* **2022,** 126, (25), 10584–10592.

19. Lu, F.; Sun, Z.; Wu, S.; Liu, W.-T. Bond additivity model for anisotropic second-harmonic generation from two-dimensional honeycomb lattices. *Opt. Lett.* **2020,** 45, (2), 268-271.